Research Article Vol. 60, No. 8 / 10 March 2021 / Applied Optics 2127

applied optics

Improvement of a computer-aided alignment algorithm for the nonsymmetric off-axis reflective telescope

Xu He,[1,*] Jing Luo,[1] Jinxin Wang,[1,2] Xiaohui Zhang,[1] and Yichen Liu[1]

[1]Changchun Institute of Optics, Fine Mechanics and Physics, Chinese Academy of Sciences, Changchun 130031, China
[2]Graduate University of Chinese Academy of Sciences, Beijing 100039, China
*Corresponding author: hexu_ciomp@sina.com

Received 9 November 2020; revised 4 February 2021; accepted 8 February 2021; posted 9 February 2021 (Doc. ID 413533); published 2 March 2021

Due to complications of the off-axis three-mirror anastigmat (TMA) telescope, each optical element in the off-axis TMA telescope is introduced with theoretical eccentricity and tilt. Moreover, the introduction of freeform surfaces and other optical elements with complex surface features generally causes the initial alignment accuracy of the optical path to be low. A large initial alignment error amplifies the sensitivity of the misalignment calculation accuracy to the measurement error of the Zernike coefficient, resulting in difficulty obtaining convergence results for a computer-aided alignment algorithm. Considering the above issues, the alignment sensitivity of each component in the optical path is analyzed in this. The large conditional number of the sensitivity matrix results in poor algorithm robustness. Thus, an adaptive damping factor least-squares algorithm model is proposed and derived to improve the efficiency of the classical least-squares algorithm. A method for piecewise optimization of the damping factor is also deduced. Experiments based on a 0.6 m off-axis TMA telescope verify the effectiveness of the algorithm. Simulation and integration experiments show that the proposed method can reduce the accuracy requirements of the initial alignment and improve the adaptability of Zernike coefficient measurement noise. The alignment procedure is carried out for three iterations, and the average of the five field-of-view wave aberration values is enhanced from 2.1λ (RMS; λ = 632.8 nm) to 0.09λ (average). The improved algorithm can solve the large initial alignment error of a nonsymmetrical off-axis reflective optical system with a freeform surface as well as the problem of the low success rate of the misalignment value due to low Zernike coefficient measurement accuracy.

https://doi.org/10.1364/AO.413533

1. INTRODUCTION

Space astronomical telescopes tend to be developed nowadays with an increased aperture and field of view (FOV), so in designing an optical system, it is becoming increasingly complex to realize the optical survey while also achieving increased resolution and limiting the detection depth [1–3]. The optical path of the telescope is further complicated in the off-axis three-mirror anastigmat (TMA) system and has evolved into a nonsymmetric off-axis optical path with a large tilt and eccentricity between the optical axes of each optical surface in the path [4]. The introduction of nonsymmetric optical surfaces, such as freeform surfaces, creates challenges for the optical alignment [5,6]. The optical integration steps for such telescopes generally include the initial placement of components and the subsequent computer-aided alignment (CAA). In solving the misalignment using the nodal aberration theory (NAT), a sensitivity matrix algorithm based on the numerical proxy model does not need to consider the analytical expression in the mathematical model when the misalignment of freeform surfaces or other complex surface components is located in a non-pupil position. Therefore, the sensitivity matrix algorithm has greater flexibility than an algorithm based on NAT. However, considering that the sensitivity matrix algorithm simplifies the complex mathematical relationship between the misalignment and the Zernike coefficient of the wavefront to a linear relation [7], the nonlinear error of the algorithm is large when the initial alignment procedure introduces an excessive residual misalignment. This characteristic has the effect that a small amount of measurement noise of the Zernike coefficient in the CAA procedure will cause the iterative process to have difficulty converging, resulting in a low probability of obtaining a global optimized solution [8].

Many studies on the numerical proxy model are carried out to calculate the misalignment. The CAA experiment and verification procedure were carried out on the ground before the Hubble space telescope was repaired in orbit to ensure the success of the on-orbit alignment. This work was completed by

J. P. McGuire of the Jet Propulsion Laboratory of the California Institute of Technology and G. F. Hartig of the Space Telescope Science Institute [9–12]. The company REOSC-SFIM has conducted engineering and experimental research for the CAA technology of a high-resolution space telescope [13]. Velluet *et al.* used the detection results of the Shack–Hartmann wavefront sensor to successfully eliminate the eccentric aberration caused by component displacement [14]. The CAA technology also enabled the off-axis TMA system to be developed, from theoretical design to practical application. The Ball company had made efforts in vain to realize the initial alignment procedure (wave aberration reaches approximately 1 λ) of its off-axis TMA telescope on the Quick Bird satellite during the integration steps. However, with the help of the CAA technology, the improvement of the wave aberration from 1 λ to 0.05 λ (RMS; λ = 632.8 nm) only took a week [15]. Yang and colleagues of CIOMP have applied the sensitivity matrix algorithm to the alignment of a TMA telescope with a focal length of 6 m [16,17]. They found that in the sensitivity matrix algorithm, the mathematical model is greatly affected by the nonlinearity, and the convergence speed is slow when applied to an off-axis TMA system, with large initial misalignment. The installation and the analysis module integrated by the well-known optical design software Code V also use the sensitivity matrix algorithm. However, some studies show that the software has low accuracy when the misalignment of optical components is larger than the design tolerance because of the remarkable nonlinear relationship between the Zernike coefficient characterizing the system's wave aberration and the amount of misalignment. Compared with an off-axis TMA system, a large-diameter nonsymmetric off-axis optical system is difficult to integrate and align [18,19]. Considering this issue, alignment technology based on the NAT was proposed and practically applied. However, a freeform surface is extremely complicated when located at a non-pupil position of an optical system, and an algorithm for solving the misalignment using the above NAT ideas is difficult to construct [20]. At the same time, there is no valid report (to our knowledge) of the use of the sensitivity matrix method in a CAA procedure when aligning a nonsymmetric off-axis optical system with a freeform surface.

The current initial positioning residual component errors of components are mostly based on the principle of the transfer of mechanical characteristics of optical components. The transmission relationship between mechanical characteristics and optical parameters is generally measured using the self-collimating theodolite or laser tracker. The initial alignment of the relative positions and the angle between optical components is based on the above measurement results. For an optical telescope with a scale of 5 m^3, the existing method introduces a misalignment residue with an eccentricity of 0.5–1 mm and a tilt of 0.05° [21]. If the relative error between the optical surface created by optical manufacturing and the mechanical references of the components (such as off-axis amount and position) is considered, the above initial positioning error also increases by 1–2 times [22]. In addition, for a nonsymmetric off-axis optical system with a freeform surface, the surface does not have the traditional rotational symmetry center due to the introduction of eccentricity and tilt between the optical axes of the surface in the path by optical design [23,24]. The above factors further reduce the accuracy of the initial placement procedure, which brings great difficulties to the subsequent CAA step and greatly reduces the accuracy of the misalignment calculated by using the traditional sensitivity matrix algorithm.

Recent studies indicate that considering the measurement noise of the Zernike coefficient, convergent results under the existing accuracy of the initial placement procedure for a nonsymmetric off-axis telescope are difficult to obtain by using a misalignment solving algorithm directly based on the sensitivity matrix. This paper addresses the above issues, analyzes the reasons for the large error in the calculation of the misalignment of a nonsymmetric off-axis optical system, and improves the algorithm accordingly. The piecewise solution and the injection of damping factors are proposed to keep the algorithm from falling into a local optimal iteration error. Then the improved algorithm is used in the alignment of a nonsymmetric off-axis optical system with an aperture of 0.6 m and a 1.1° × 1.1° FOV. The improvement in the Zernike coefficient measurement error tolerance and the effectiveness of the algorithm are verified through simulation and experiment.

2. INTRODUCTION OF THE NONSYSMMETRIC OFF-AXIS TELESCOPE

A nonsymmetric off-axis reflective optical telescope with a focal length of 6 m, an aperture of 0.6 m, and a 1.1° × 1.1° FOV is used as an example to discuss the misalignment solving algorithm.

The optical system is composed of a primary mirror (M1), a second mirror (M2), and a third mirror (M3). This telescope is designed for the verification of the key technology of the space-based optical survey. It is complicated due to the classical off-axis TMA optical path intended to expand the FOV in the meridional direction and reduce aberration. The optical design rotates and translates the optical axis of M2 and M3 relative to M1. M3 in the non-pupil position is designed to become a freeform surface fitted by Zernike coefficients. In accordance with the optical design parameters, the optical path and the wavefronts of five typical FOVs are shown in Figs. 1 and 2, respectively.

The axis eccentricity is 29.0464 mm between M1 and M3 and 8.2611 mm between M1 and M2. The tilt of the axis between M1 and M2 is 1°. The off-axis amounts of M1, M3, and M2 are −460, 40, and −70 mm, respectively. A local coordinate system is established to facilitate the transfer of the calculated misalignment to the adjustment of the optical

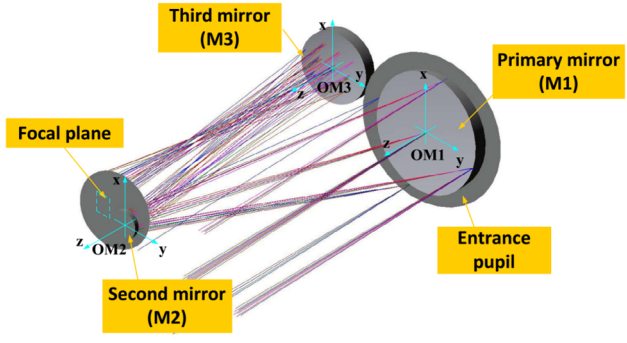

Fig. 1. Schematic of the optical path of the nonsymmetric off-axis telescope defining the coordinates.

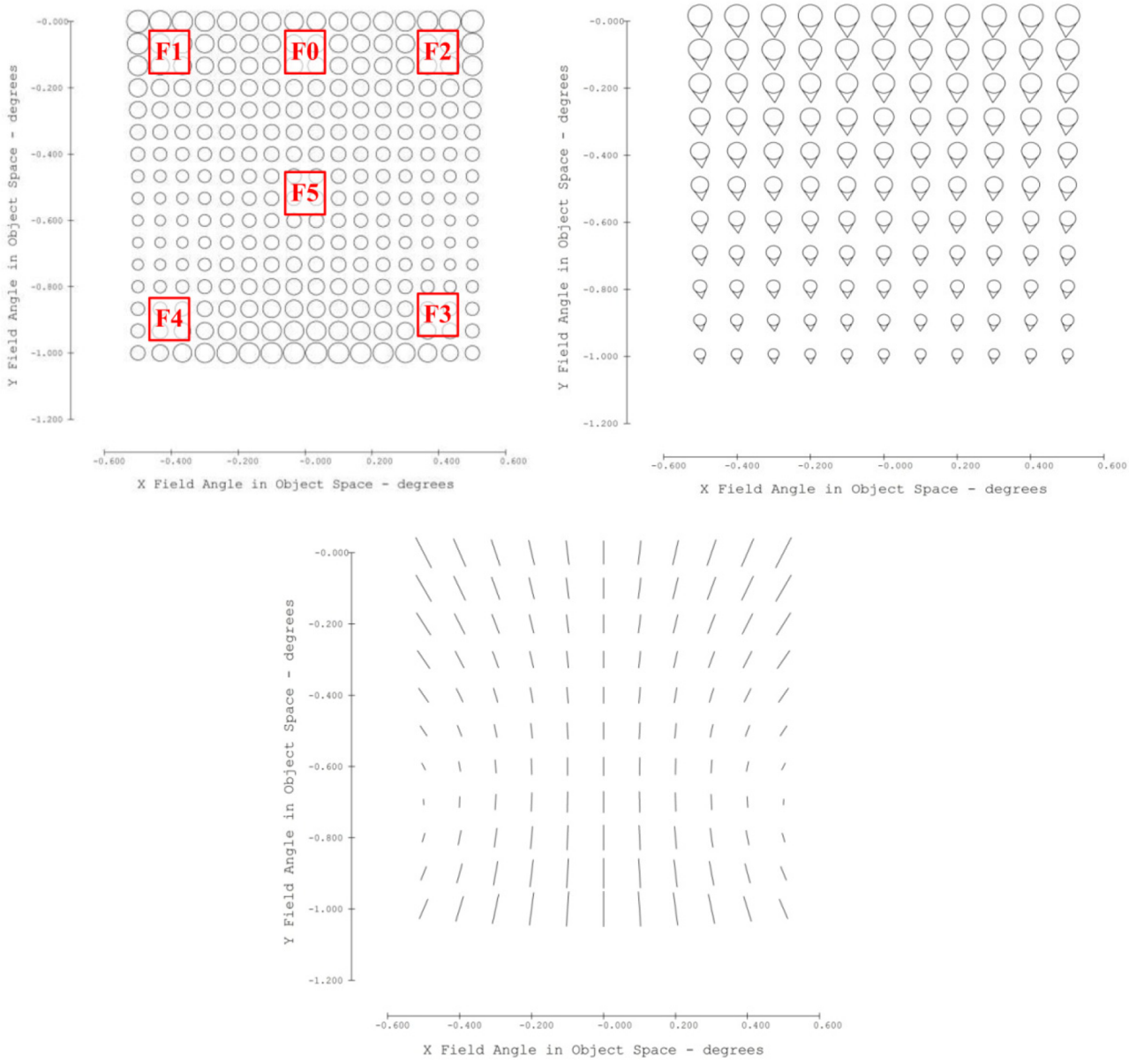

Fig. 2. Distribution of the aberrations of wavefront, coma (C7/8), and astigmatism (C5/6) in each FOV without misalignment.

components. The origin of the coordinate system is the vertex of each optical surface relocated to the geometric center of the components. The z-axis vector is parallel to the optical axis direction of each surface. The x-axis vector is defined as the meridional direction. According to the right-hand rule, the local optical coordinate systems of M1, M2, and M3 can be determined separately: OPM, OSM, and OTM, respectively. The misalignment is defined in this paper as the scalar deviation of the local coordinate system of each optical surface from the theoretical value. Figure 2 shows the exit pupil aberrations and the corresponding Fringe Zernike coefficients (hereinafter referred to as Zernike coefficients) of five typical FOVs (without FOV 0) when the optical system has no misalignment (C4, C5, C6, and C7 represent Astig x, Astig y, Coma x, and Coma y, respectively). The values are shown in Table 1 without considering the surface profile error of the three mirrors.

Table 1. WFE (RMS) and Zernike Coefficient C4/5 and C6/7 of Five Typical FOVs without Misalignment

	F0	F1	F2	F3	F4
WFE	0.0371	0.0575	0.0575	0.0452	0.0575
$C4/5_{average}$	–0.0281	–0.0795	0.0131	–0.0498	0.0015
$C6/7_{average}$	0.0320	0.0402	0.0478	0.0236	0.0170

The surface shape errors of M1, M2, and M3, measured using the interferometer and compensators, are added to the optical design, and the wavefront aberration of each FOV of the optical system is fitted again. The simulation results of the C5/6 and C7/8 terms of the Zernike coefficient and the RMS distribution in each FOV are shown in Fig. 3.

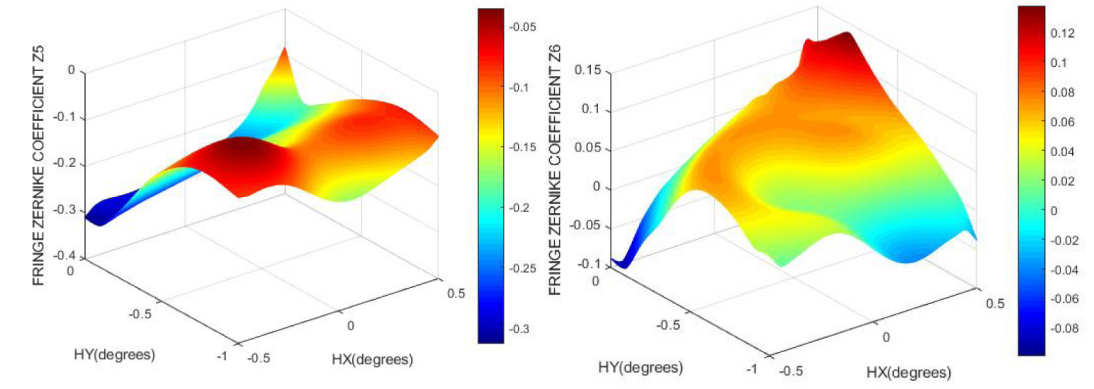

(a)

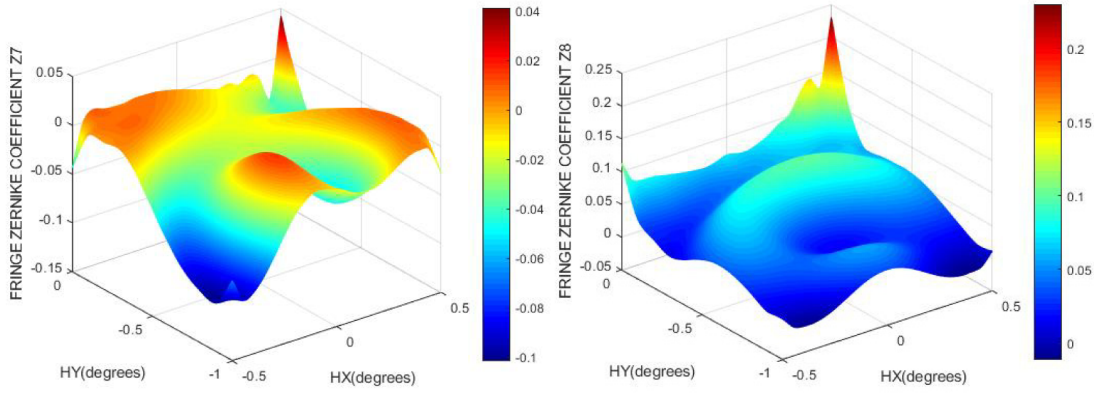

(b)

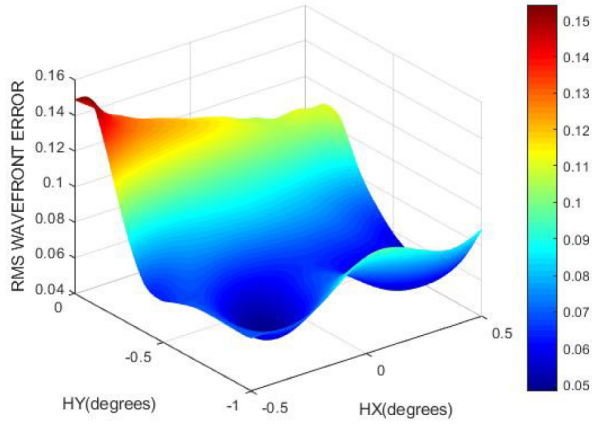

(c)

Fig. 3. Distribution of the aberrations of wavefront, coma (C7/8), and astigmatism (C5/6) in each FOV with the addition of surface shape errors. (a) Distribution of the x- and y-direction astigmatism (C5/6) in each FOV with the surface shape errors of the mirrors, (b) distribution of the x- and y-direction coma (C7/8) in each FOV with the surface shape errors of the mirrors, (c) distribution of the wavefront aberration (RMS values) in each FOV with the surface shape errors of the mirrors.

3. SENSITIVITY ANALYSIS OF MISALIGNMENT

The alignment strategy and steps should first be determined to complete the integration process of the nonsymmetric off-axis telescope shown in Fig. 1. The misalignment sensitivity order of each single surface and the coupling relationship between the high-sensitivity misalignment dimensions can provide basis for the determination of the alignment strategy and steps, as well as the improvement of the algorithm for solving the misalignment value. Let the three-dimensional relocation (including two-dimensional eccentricity and along-axis misalignments) between the local coordinate systems of the surfaces be represented by XD, YD, and ZD. The misalignment of the three-dimensional rotation direction (including two-dimensional tilt and one-dimensional roll direction misalignment) around the axes is represented by XR, YR, and ZR.

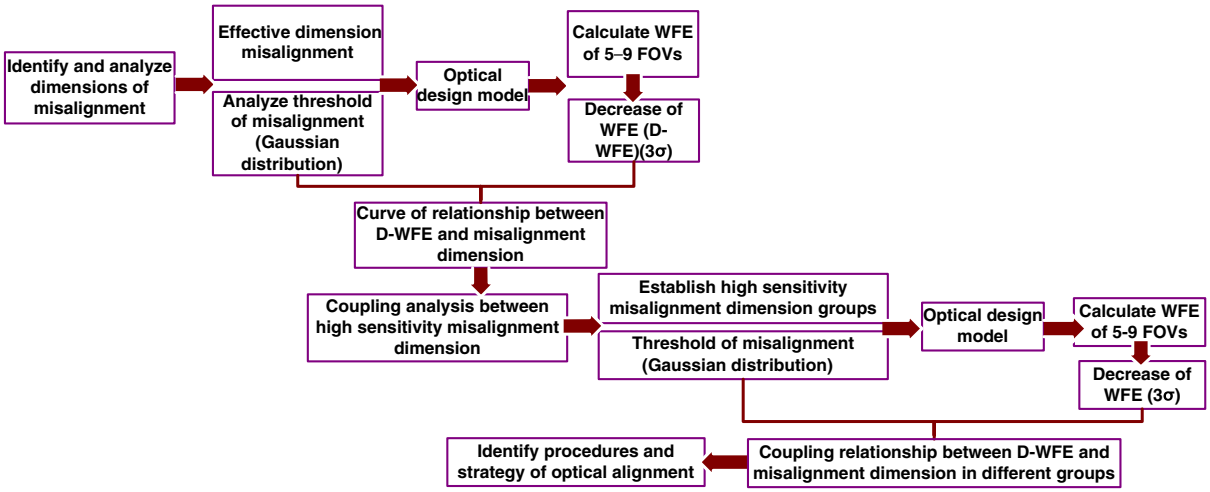

Fig. 4. Steps and methods for the sensitivity analysis of misalignment.D-WFE, decrease of the wave-front error.

Table 2. Threshold Ranges of Misalignment for the Nonsymmetric Off-Axis Telescope Used in the Sensitivity Analysis

	XD	YD	ZD	XR	YR	ZR
M1	±0.5 mm	±0.5 mm	±0.5 mm	±180″	±180″	±180″
M2	±0.5 mm	±0.5 mm	±0.5 mm	±180″	±180″	±180″
M3	±0.5 mm	±0.5 mm	±0.5 mm	±180″	±180″	±180″

The input threshold used in the misalignment sensitivity analysis comes from the mean square sum of the two error sources. One part of the error comes from the residuals of the initial placement procedure with the current method, and another part of the error comes from the relative error between the optical surface of the optical components and the mechanical body. The thresholds of misalignment are shown in Table 2, and the sensitivity analysis method of misalignment is shown as a block diagram in Fig. 4.

The simulation results in Fig. 5 show that M2 in the off-axis optical system has the highest sensitivity to the x-direction misalignment, and M1's sensitivity to the z-direction misalignment is the second highest. M1's sensitivity to the misalignment in the x-tilt and y-tilt directions and M1's sensitivity to the y-direction misalignment are also relatively high. Considering that the misalignment sensitivity of M1 is relatively high and the volume and mass of M1 are relatively large, adjustment with high precision is difficult. Therefore, M1 should be used as the alignment reference, and M2 and M3 should be aligned as compensators to correct misalignment wavefront aberrations. In addition to M1, M2 also has high sensitivity to the misalignment in the z direction. Moreover, the misalignment sensitivity values of the rotation of M2 around the x axis, the rotation of M3 around the x axis, and the rotation of M2 around the y axis are relatively high. Therefore, the coupling analysis is performed on the basis of the univariate misalignment sensitivity analysis. The coupling analysis group includes M2 ZD–XR, M2 ZD–YR, and M2 XR–YR, as well as M2 ZD–M3 XR, M2

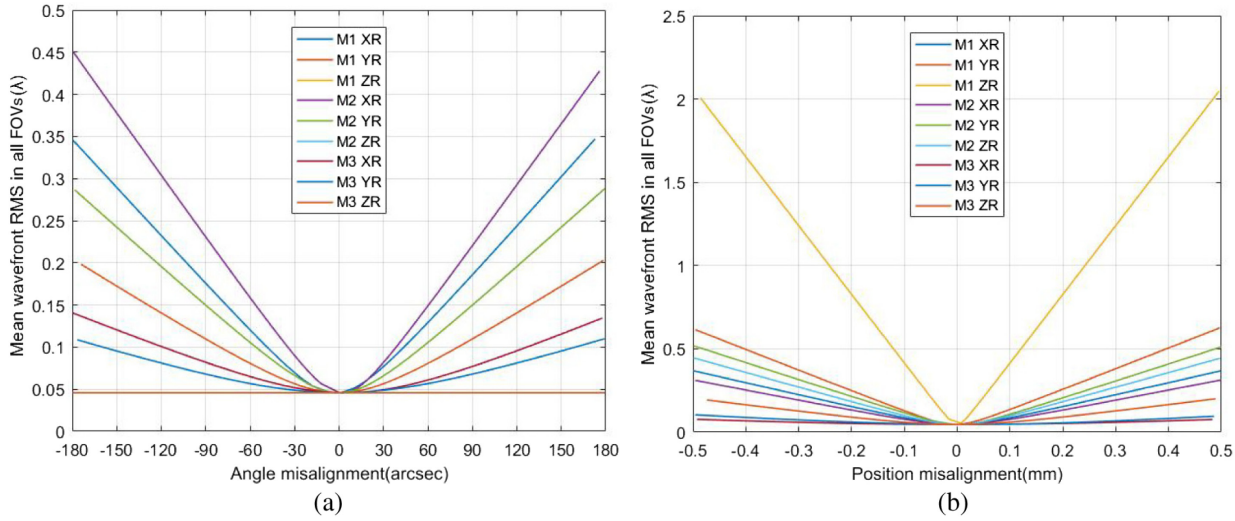

Fig. 5. Misalignment sensitivities of M1, M2, and M3 in different dimensions are displayed by multiple sets of curves. (a) Sensitivity analysis of the position errors of M1, M2, and M3, (b) sensitivity analysis of the tilt errors of M1, M2, and M3.

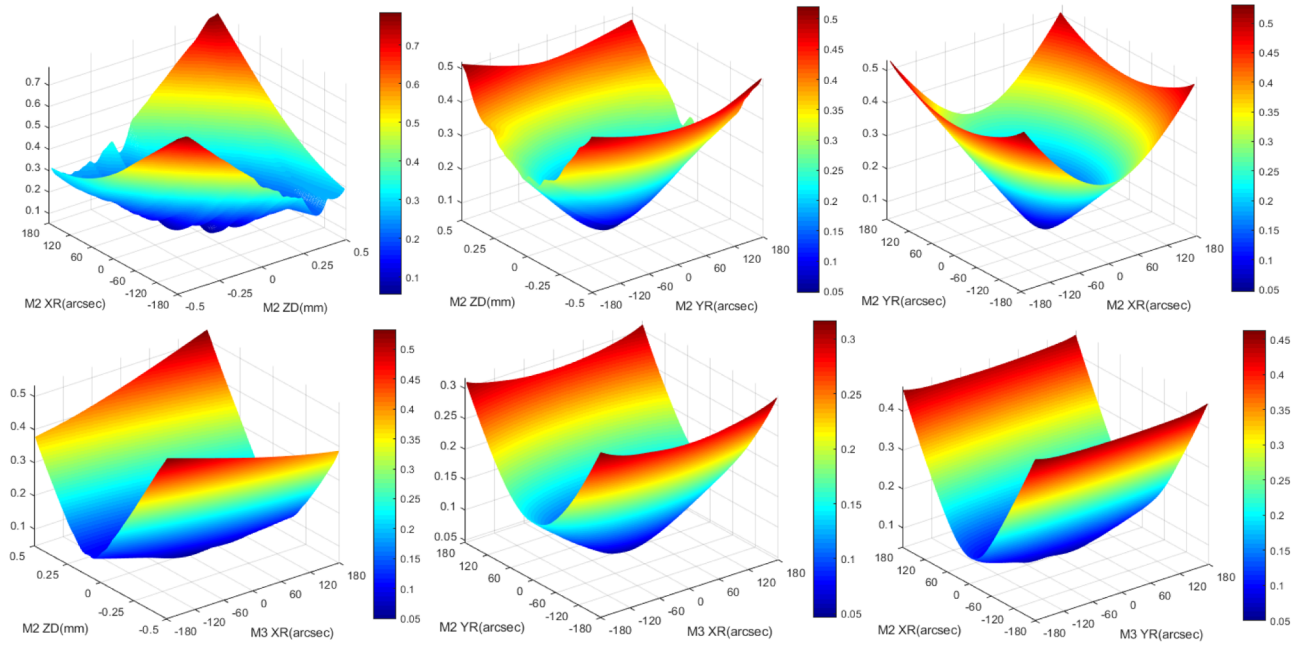

Fig. 6. Coupling analysis results between dimensions with high sensitivity to misalignment are shown as surface graphs.

XR–M3 YR, and M2 YR–M3 XR. The results of the coupling misalignment sensitivity analysis are shown in Fig. 6.

As shown in Fig. 4, the numerical relationship between the misalignment of each freedom dimension of each optical component and the exit pupil wavefront error (WFE; average value) of five typical FOVs is determined. Based on this, the sequence of the univariate of misalignment sensitivity is determined. Two or more misalignment dimensions with high sensitivity are combined. The coupling relationship between the coupling misalignment and the aberration degeneration of the exit pupil in five typical FOVs is obtained. The above numerical relationship is established on the basis of the mathematical–optical integrated simulation. The input misalignments of the simulation come from the normal distribution of random numbers corresponding to each misalignment dimension of the thresholds (Table 2). Based on a Monte Carlo simulation, the average value of the WFE degradation of the five FOVs corresponding to the 3σ range can be obtained. The Monte Carlo simulation takes the boundary value corresponding to the 3σ range as the simulation result of the univariate and the coupling analysis.

The univariate analysis results are shown in Fig. 5. The abscissa represents the misalignment thresholds, and the ordinate is the average value of the WFE (RMS) degradation in five typical FOVs. The misalignments entered in the simulations come from 500 sets of randomly distributed misalignments that are normally distributed within the thresholds of each dimension in Table 2. The simulation algorithm calculates the average value of the aberration degradation of each FOV, and the misalignment–sensitivity curve is constructed on the basis of the above calculation.

The misalignment sensitivity analysis in Figs. 5 and 6 can guide the establishment of a CAA model of the optical system. First, in the case where M2 is misaligned along the z axis, when the other dimensions of M2 or M3 are misaligned, the misalignment sensitivity of M2 along the z direction does not change remarkably. This characteristic indicates that the coupling degrees of M2's misalignment in the z direction and other dimensions are extremely low, which leads to a reduction in the condition number of the sensitivity matrix. Second, when misalignments of M2 are present in the x direction or y direction, the amount of aberration reduction in each FOV of the system exhibits quadratic surface distribution characteristics. In addition, a coupling between the x-direction rotation of M2 and the x-direction rotation of M3 is observed. Third, a coupling between the misalignment of M3 around the x-direction rotation and the misalignment of M2 around the y-direction rotation is observed. These findings indicate that the condition number of the sensitivity matrix composed of the abovementioned misalignments with a coupling relationship is better. Finally, the coupling between the z-direction misalignment of M2 and the eccentricity in the x direction and y direction is weak and can be supplemented by the eccentricity in the above two directions. The same is true for M3.

4. IMPROVEMENT OF THE ALGORITHM FOR SOLVING THE MISALIGNMENT

Based on the analysis of the misalignment sensitivity, the classic sensitivity matrix–least-squares algorithm [25,26] can be improved. The mathematical model of the function is based on the Taylor function multivariate theorem. The wavefront aberrations of the jth ($j = 1 - 5$) FOV of the optical system can be expanded into the Zernike coefficient polynomial form. Therefore, the i item Zernike coefficient of the j FOVs can be expressed as

$$W(\rho,\theta)=C_i^j(A)=C_i^j(B+\Delta m_n)$$
$$=\sum_{p=0}^{m}\frac{1}{p!}\left(\sum_{q=1}^{n}\Delta m_q\frac{\partial}{\partial x_q}\right)^p C_i^j(B)+R_{N.m}(\Delta M). \tag{1}$$

In Eq. (1),

$$|A|=(x_1,x_2,x_3\cdots x_n)=|B|+\Delta m_n. \tag{2}$$

Matrix $|A|$ represents any condition of misalignment, which includes the efficient degrees of freedom of misalignment of all the optical surfaces. Matrix $|B|$ in Eq. (2) represents the position and the angle of each dimension of each component in the optical path under the local coordinate system in the optical design state:

$$|B|=(x_{01},x_{02},x_{03}\cdots x_{0n}). \tag{3}$$

In each procedure, the misalignments corresponding to the dimension are separately introduced under the local coordinate system of each optical component. The vector ΔM represents the misalignments of n degrees of freedom corresponding to every alignment procedure:

$$\Delta M=(\Delta m_1,\Delta m_2,\Delta m_3\cdots\Delta m_n). \tag{4}$$

$R_{N,m}(\Delta M)$ is the remainder term. The linear approximation of Eq. (1) and the first-order expansion (i.e., order $p=1$) are performed, and the following is obtained:

$$W(\rho,\theta)=C_i^j(B+\Delta m_n)=C_i^j(B)$$
$$+\left(\sum_{q=1}^{n}\Delta m_q\frac{\partial}{\partial x_q}\right)C_i^j(B)+R_{N.m}(\Delta M)$$
$$=C_i^j(B)+\sum_{q=1}^{n}\Delta m_q\frac{\partial C_i^j(B)}{\partial x_q}. \tag{5}$$

Equation (5) can be transformed into a matrix form:

$$\begin{bmatrix}C_1^1(B+\Delta m_n)\\ \vdots\\ C_i^j(B+\Delta m_n)\\ \vdots\end{bmatrix}=\begin{bmatrix}C_1^1(B)\\ \vdots\\ C_i^j(B)\\ \vdots\end{bmatrix}$$
$$+\begin{bmatrix}\frac{\partial C_1^1(B)}{\partial x_1} & \frac{\partial C_1^1(B)}{\partial x_2} & \cdots & \frac{\partial C_1^1(B)}{\partial x_n}\\ \vdots & \vdots & \vdots & \vdots\\ \frac{\partial C_i^j(B)}{\partial x_1} & \frac{\partial C_i^j(B)}{\partial x_2} & \cdots & \frac{\partial C_i^j(B)}{\partial x_n}\\ \vdots & \vdots & \vdots & \vdots\end{bmatrix}\begin{bmatrix}\Delta m_1\\ \Delta m_2\\ \vdots\\ \Delta m_n\end{bmatrix}. \tag{6}$$

$C_i^j(B)$ can be obtained in accordance with the optical design. $C_i^j(B+\Delta m_n)$ can be measured in each FOV by using a commercial interferometer. Based on the measured values, an overdetermined system of equations for solving the misalignments (Δm_n) can be established. The evaluation function (m) can be defined for the system of equations. When the residual sum of the squares of each aberration of the system is the smallest, the wavefront aberration results of the optical system are closest to the theoretical design value. Therefore, the matrix form of the evaluation function and its least-squares solution can be expressed as

$$\eta(\Delta m_n)=\sum_{i=1}^{Z_n}\left(\left[\frac{\delta C_i^j(B)}{\delta x_n}\right]\cdot[\Delta m_n]-\Delta C_i^j(B+\Delta)-\delta_i^j\right)^2, \tag{7}$$

$$\nabla\eta(\Delta m_n)=0. \tag{8}$$

The prerequisite for the convergence of each dimension of the misalignments calculated using Eq. (8) is the square matrix in its normal equation, which is nonsingular and is given by

$$\left[\frac{\delta C_i^j(B)}{\delta x_n}\right]^T\left[\frac{\delta C_i^j(B)}{\delta x_n}\right]. \tag{9}$$

However, according to the sensitivity analysis results in Section 3, Eq. (8) is difficult to solve, because within the range of misalignment (Table 2), a large nonlinearity is observed between the wavefront aberration deterioration and the amount of misalignment (Fig. 5). The existence of the measurement error (δ_i^j) of the Zernike coefficient makes it difficult to obtain the convergence solution of Eq. (8). The difference in the sensitivity between the misalignments of various dimensions is large (Fig. 5), resulting in a large condition number of the sensitivity matrix and thus an ill-conditioned matrix. Therefore, the misalignment solving equation constructed on this basis falls into the local optimal solution and cannot obtain global convergence. Finally, clear coupling characteristics are observed between the misalignment dimensions (Fig. 6), which makes it difficult to obtain convergent solutions that make the wavefront aberrations return to the optical design result under some misalignment combinations of Eq. (8).

After adding the damping factors (P_0, a vector quantity) to the process of the solution result $[\Delta m_n]$, the evaluation function can be improved to the form of Eq. (10) below. After adding the vector quantity of damping factors, the equation can be prevented from prematurely diverging during the iteration process, the condition number of the equation can be improved, and the amplification effect of the measurement noise of the Zernike coefficient on the nonlinear equivalent error can be alleviated:

$$\eta(\Delta m_n)=\sum_{i=1}^{Z_n}\left(\left[\frac{\delta C_i^j(B)}{\delta x_n}\right]\cdot[\Delta m_n]-\Delta C_i^j(B+\Delta)-\delta_i^j\right)^2$$
$$+P_0^2[\Delta m_n][\Delta m_n]^T. \tag{10}$$

Equation (10) is integrated into Eq. (8) to calculate the misalignments in each dimension. However, the simple introduction of damping factors into the equations for solving the misalignment can also lead to other problems. For example, if the damping factor is large, the step size of the misalignment calculated using the equations will be small, and the small misalignment value calculated in each step is easily suppressed by

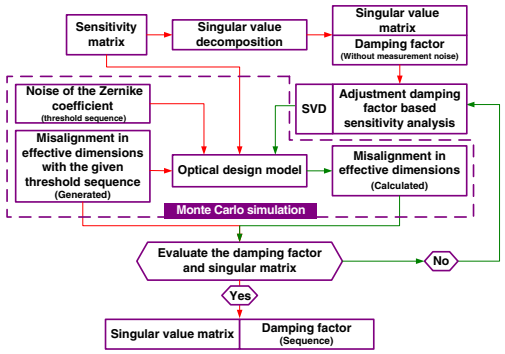

Fig. 7. Block diagram representing the algorithm of the damping factor sequence corresponding to different misalignment intervals.

the cross talk error of the adjustment stage. This phenomenon greatly reduces the efficiency and the success rate of the alignment procedure. Moreover, if the damping factor is small, the problem of the equations falling into the local optimal solution, arising from the measurement noise of the Zernike coefficient, cannot be eliminated when the initial misalignment is large.

Therefore, the idea of a piecewise adaptive damping factor is proposed to solve this issue. The calculation algorithm of the adaptive damping factor sequence based on the singular value decomposition (SVD) method and Monte Carlo simulation is shown in Fig. 7. The singular value matrix without Zernike coefficient measurement noise is obtained first, and the damping factor of the Zernike coefficient without measurement noise is obtained simultaneously. In the second step, the values $\lambda/10$, $\lambda/15$, $\lambda/20$, $\lambda/25 \ldots \lambda/100$ [δ_j^i in Equation (7)] are used as the thresholds of the measurement noise of the Zernike coefficient, and the measurement noise is normally distributed in the simulation. An exhaustive iterative algorithm is used to build loops (green line). The calculation result of the misalignment of a single iteration is no less than one-third of the total misalignment (based on the analysis results of the misalignment sensitivity), which is used as the evaluation standard for determining whether the damping factor is appropriate in the loop algorithm. The combined sequence of damping factors corresponding to different Zernike coefficient measurement noise thresholds and initial alignment errors can be calculated.

Based on the algorithm shown in Fig. 7, an improved least-squares algorithm for the piecewise adaptive damping factor injection is proposed. The block diagram of the misalignment calculation algorithm based on the segmented injection of the damping factor sequence is shown in Fig. 8. The algorithm and steps for solving equations based on the damping factor sequence are shown in this figure. The key idea of the adaptive search algorithm for damping factors is to segment the misalignment threshold interval on the basis of the analysis results of the misalignment sensitivity. Under different subintervals and Zernike coefficient measurement noise conditions, a series of damping factors that maximize the convergence efficiency of Eq. (9) is determined. Thus, a damping factor sequence corresponding to the segmented misalignment intervals is obtained and is used for the alignment procedure. Misalignment intervals are based on reduction in the wavefront aberrations of each FOV.

In the alignment experiment, when the distribution interval of the random noise of the Zernike coefficient measurement is tested, different damping factors can be injected into the algorithm in accordance with the value of the misalignment solved previously to quickly obtain convergent calculation results at different misalignment intervals. The 0.6 m nonsymmetric

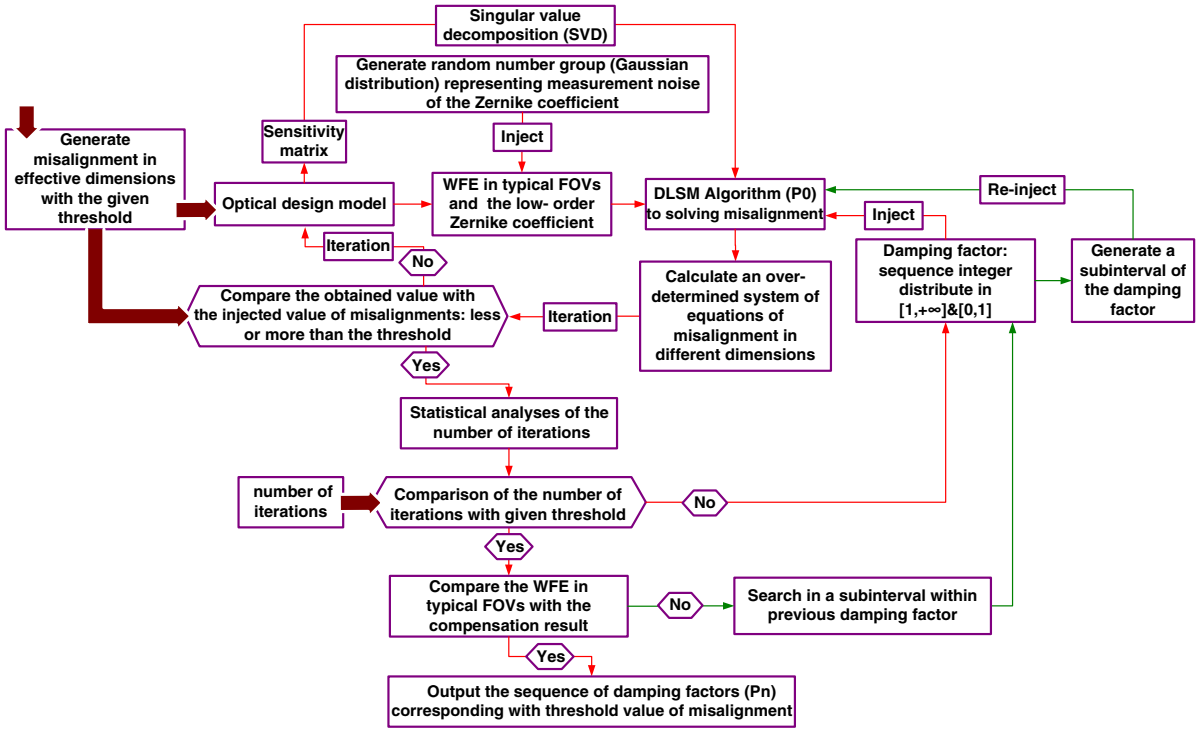

Fig. 8. Functional block diagram expressing the adaptive analysis algorithm of the damping factors sequence corresponding to different misalignment intervals.

Table 3. Singular Value Matrix and Damping Factor Sequence Corresponding to Different Zernike Coefficient Measurement Noise Values and Different Misalignment Thresholds (λ = 632.8 nm)

Initial Misalignment	Noise of Zernike Coefficient	Singular Value Matrix (Diagonal Matrix)										Damping Factor
SMXD/ ±0.5 mm	0	0.035	0.036	0.139	0.139	3.776	4.999	1.854	1.263	0.512	0.109	**0.05**
SMYD/ ±0.05°	λ/10	0.035	0.036	0.138	0.138	0.537	0.272	0.053	0.036	0.014	0.003	**0.61**
SMZD	λ/20	0.035	0.036	0.138	0.138	1.285	0.759	0.157	0.105	0.042	0.009	**0.35**
SMXR/	λ/40	0.035	0.036	0.139	0.139	2.490	2.007	0.476	0.320	0.128	0.003	**0.21**
SMYR	λ/60	0.035	0.036	0.139	0.139	3.107	3.084	0.841	0.566	0.228	0.048	**0.15**
SMXD/ ±0.1 mm	0	0.035	0.036	0.138	0.138	3.773	5.000	1.854	1.263	0.512	0.109	**0.05**
SMYD/ ±0.01deg	λ/10	0.035	0.036	0.138	0.138	0.736	0.387	0.077	0.051	0.021	0.004	**0.55**
SMZD	λ/20	0.035	0.036	0.138	0.139	1.588	1.005	0.213	0.142	0.006	0.012	**0.32**
SMXR/	λ/40	0.035	0.036	0.139	0.139	3.107	3.084	0.841	0.566	0.228	0.048	**0.15**
SMYR	λ/60	0.035	0.036	0.139	0.139	3.776	5.000	1.854	1.263	0.512	0.109	**0.12**

off-axis telescope is used as an example of the damping factor sequence calculation. The misalignment of each dimension, listed in Table 2, is used as the initial alignment condition. The singular matrix is calculated when the measured noise of the Zernike coefficient is λ/10, λ/20, λ/40, λ/60. The corresponding damping factor of the first iteration is shown in Table 3. SMXD represents the eccentricity of M2 in the *x* direction, SMYD represents the eccentricity of M2 in the *y* direction, SMZD represents the defocus of M2 in the *z* direction, SMAR represents the tilt of M2 around the *x* axis, and SMBR represents the tilt of M2 around the *y* axis.

5. SIMULATION EXPERIMENT

A nonsymmetric off-axis system with a diameter of 0.6 m (Fig. 1) is used as the calculation example for the simulation experiments to verify the abovementioned misalignment calculation model. The alignment reference during the integration process is M1. The stability error of M1 is ignored during the alignment procedure.

Through the initial alignment step, the initial conditions of M2 and M3 have position and angle errors in the local coordinate system (Table 4). The Monte Carlo simulation is carried out within the misalignment thresholds given in Table 4. A total of 300 sets of normally distributed random numbers are generated within the misalignment thresholds of each dimension of M2 and M3, representing 300 random misalignment conditions in the five dimensions of the two mirrors separately. After each simulation program is injected, the wavefront aberrations of the five characteristic FOVs and the corresponding first nine Zernike coefficients are extracted. The λ/20 (normal distribution) measurement noise is randomly added to the extracted Zernike coefficients. Each parameter is injected into Eq. (10) separately. After several simulation iterations, the convergence results of the misalignment in each effective dimension and the corresponding wavefront aberrations (average) can be obtained. The results of the simulated alignment are shown in Fig. 9.

Figure 9(a) shows the misalignment correction results for M2 and M3. The abscissa is the randomly generated misalignment of the normal distribution, and the ordinate represents the misalignment of M2 and M3 obtained using the improved algorithm. The red scatterplot indicates the regression of the misalignment obtained using the adaptive damping factor least-squares algorithm model (DLSM). The blue scatterplot

Table 4. Misalignment Threshold Range for the Optical Components Introduced in the Simulation Experiment Setup

	XD	YD	ZD	XR	YR
M2	±0.5 mm	±0.5 mm	±0.5 mm	±360″	±360″
M3	±0.3 mm	±0.3 mm	±0.3 mm	±360″	±360″

represents the results obtained by the classical least-squares algorithm model (LSM).

Figure 10 shows the corrected results of the wavefront aberrations of five FOVs after alignment. The ordinate represents the average wavefront aberrations of each FOV (λ = 632.8 nm), and the abscissa represents the number of simulations. The red scatterplot indicates the average value of the wavefront aberrations in the case of the 10-dimensional random misalignments of M2 and M3 after they were corrected using the DLSM. The green scatterplot indicates the average value of the wavefront aberrations of the five characteristic FOVs after being corrected using the LSM with the same order of Zernike coefficient measurement noise.

Figure 11 shows the number of iterations corresponding to the case of using a single damping factor with the Zernike coefficient measurement noise (represented by the red scatterplot, Z = 0). The ordinate represents the wavefront aberrations, and the abscissa represents the number of iterations. The scatterplots in other colors indicate the number of iterations for different damping factors. The correction results of the wavefront aberrations are shown in the ordinate.

The simulation results [Fig. 9(a)] show that the Zernike coefficient measurement noise has an increased effect on the accuracy and the convergence of the least-squares algorithm due to the high sensitivity of M2 (Fig. 5). Compared with the LSM, the piecewise DLSM is less disturbed by the Zernike coefficient measurement error. The simulation results in Fig. 9 show that the solution results obtained using the DLSM algorithm have high convergence. The simulation results in Fig. 9(b) reflect the physical basis of the misalignment calculation model, that is, through mutual compensation between the positions and the angles of the optical components. The system wavefront aberrations are corrected to the design result. The simulation results in Fig. 9(b) show the significant difference between the sensitivity of M3 and that of M2. The two-dimensional eccentricity and the misalignment along the axis of M3 can still be

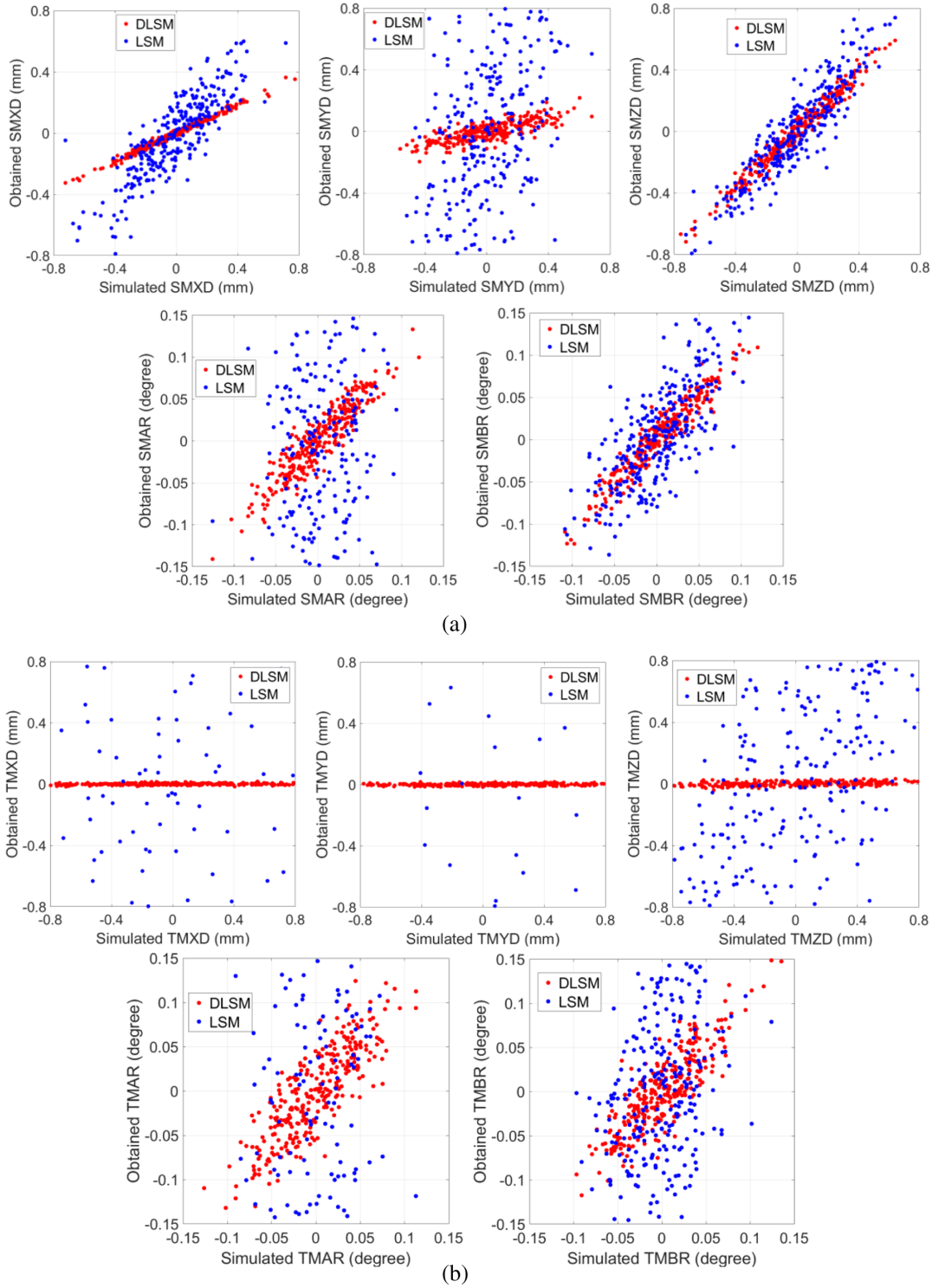

Fig. 9. Simulation results for the misalignment correction in each efficient dimension of M2 and M3. (a) Misalignment correction results of M2, (b) misalignment correction results of M3. SMXD represents the eccentricity of M2 in the x direction, SMYD represents the eccentricity of M2 in the y direction, SMZD represents the defocus of M2 in the z direction, SMAR represents the tilt of M2 around the x axis, and SMBR represents the tilt of M2 around the y axis. TMXD represents the eccentricity of M3 in the x direction, TMYD represents the eccentricity of M3 in the y direction, TMZD represents the defocus of M3 in the z direction, TMAR represents the tilt of M3 around the x axis, and TMBR represents the tilt of M3 around the y axis.

compensated by M2. Therefore, the residual misalignments that need to be corrected for M3 that are calculated using the DLSM are extremely small. However, the classical LSM cannot easily obtain a convergent solution under similar noise and initial conditions. The system wavefront aberrations are still sensitive to the two-dimensional tilt misalignments of M3 (corresponding

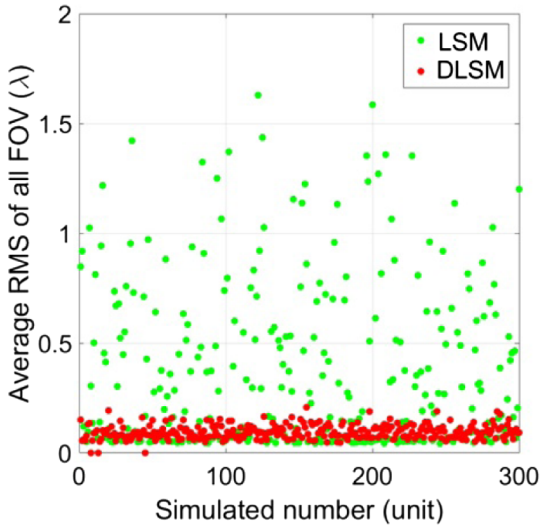

Fig. 10. Correction results for the wavefront aberration of each FOV (average value) after compensation adjustment.

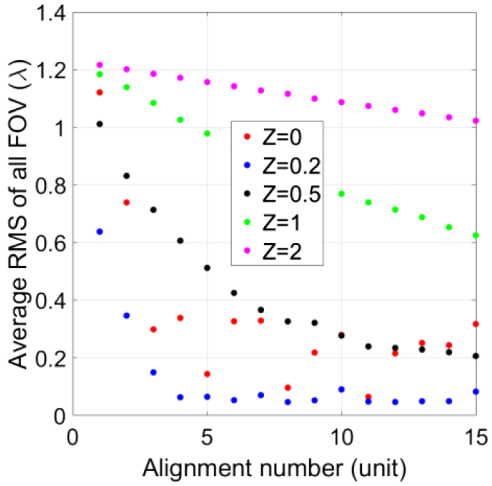

Fig. 11. Simulation results for the relationship between the number of iterative adjustments and the efficiency of the alignment.

to the simulation results in Fig. 5). When the two-dimensional misalignments exceed a certain range, completely compensating through the correction of M2 is difficult. Compared with the least-squares algorithm, the convergence of the tilt misalignment of M3 that is calculated using the DLSM is also relatively high. Figure 10 shows that the wavefront aberrations in the square FOV are effectively corrected using the improved algorithm under most circumstances. The average value of the wavefront aberrations can be corrected to $\lambda/12$ from approximately 2λ (RMS; $\lambda = 632.8$ nm). Figure 11 shows that compared with the classical least-squares algorithm, the model that includes injecting different damping factors into different misalignment intervals results in different correction effects. With the injection of a series of appropriate damping factors, the efficiency and accuracy of the solution of the misalignment can be evaluated.

In summary, compared with the classical algorithm of least squares, the improved algorithm solves the misalignments of each efficient dimension of M2 and M3 with high accuracy and a high success rate. Figures 10 and 11 show that in most cases, the misalignment can be accurately resolved and can help compensate the wavefront aberration over the whole FOV.

6. ALIGNMENT EXPERIMENT

The 0.6 m nonsymmetric off-axis telescope is used in integration and alignment experiments to verify the above simulation results and algorithms. The experiment site is shown in Fig. 12.

M1 is connected to a fixed bracket as an alignment reference. M3 and M2 are both fixed on multidimensional adjustment stages. A PI P-850 Hexapod adjustment stage is used for adjustment and positioning to improve the adjustment resolution and positioning accuracy of M2. A calibration device is used to adjust the consistency of the motion coordinate system of the adjustment stage and the local optical coordinate system of M2 and M3. The experiment uses a flat mirror with a diameter (Φ) of 700 mm and a surface accuracy of $\lambda/50$ (RMS; $\lambda = 632.8$ nm). The experiment also uses a 4D AccuFiz interferometer to measure the system's exit pupil aberrations. The experiment uses a Leica 6100 autocollimating theodolite to determine the testing FOV. The experimental optical path is a typical collimated interference optical

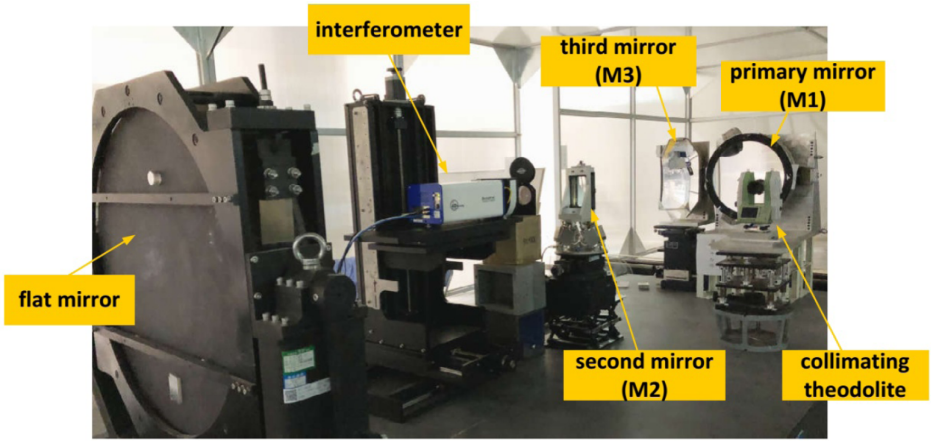

Fig. 12. Installation and alignment experiment site of the 0.6 m off-axis reflection optical system.

path. The initial rough positioning step uses multi-CGH (computer-generated hologram) for the direct transmission optical reference, which improves the initial positioning accuracy of the off-axis system. Figure 12 shows the CAA experiment site and the composition of the experimental optical path.

Before the CAA procedure begins, the Zernike coefficient measurement noise of the laboratory needs to be obtained.

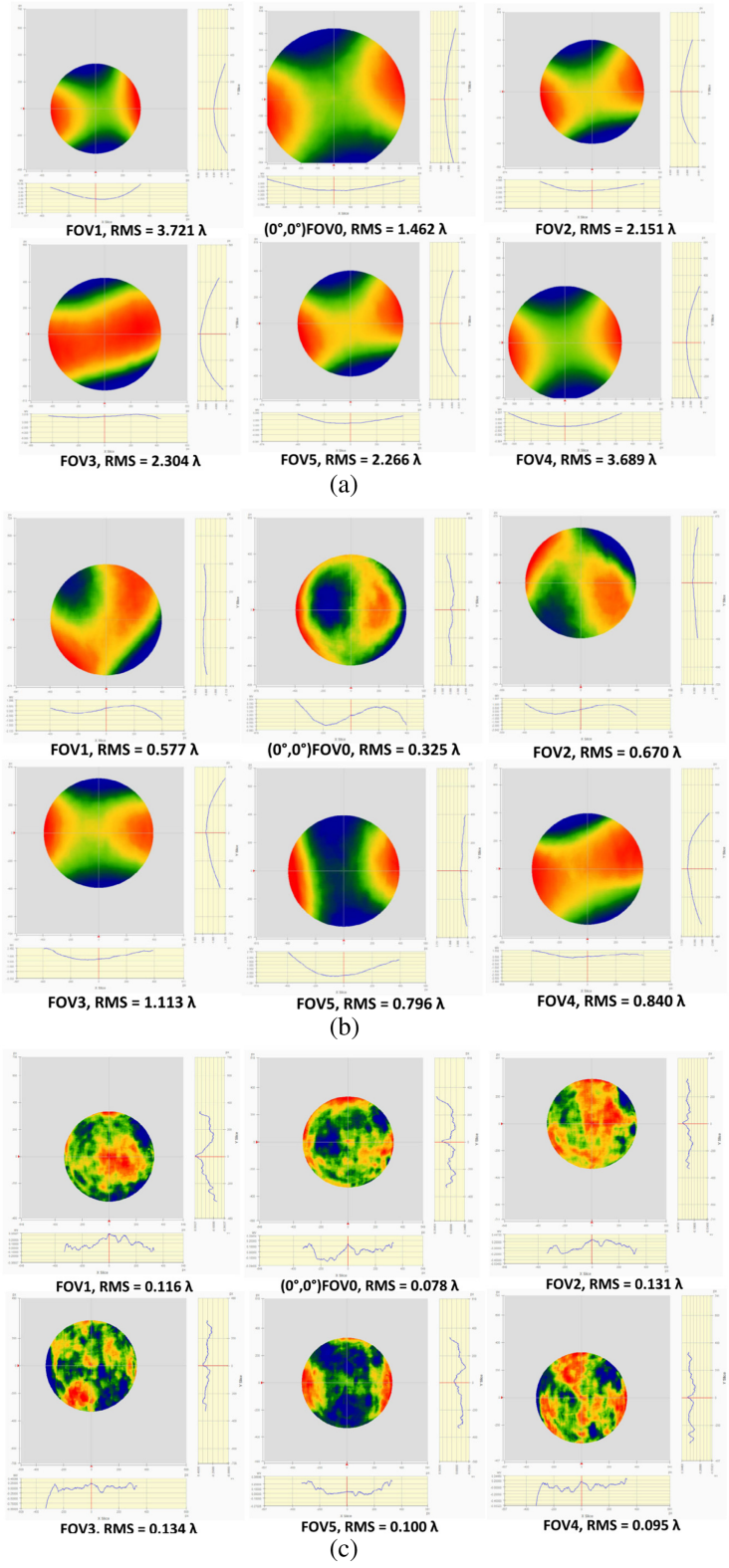

Fig. 13. Measurement results for the wavefront aberrations in six FOVs after three iterative alignments ($\lambda = 632.8$ nm). (a) Measurement results after the initial alignment, (b) measurement results after the first iterative alignment, (c) measurement results after the second iterative alignment.

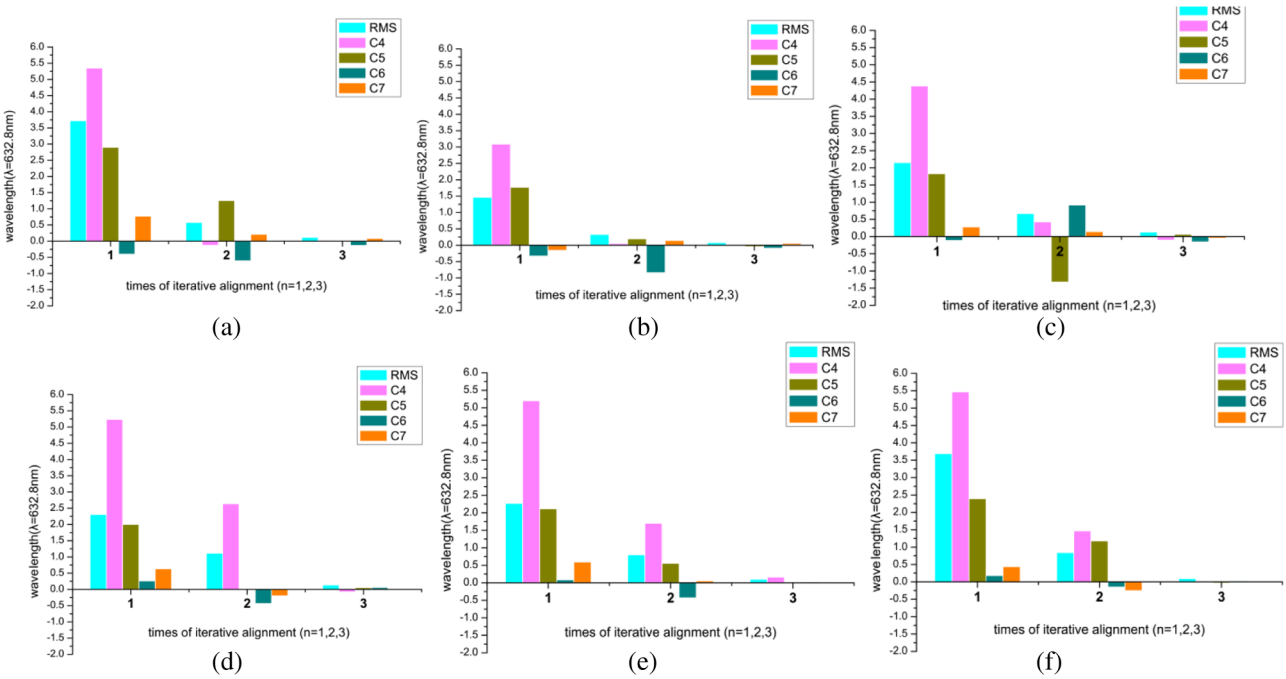

Fig. 14. Iterative convergence of the RMS and the Zernike coefficients in six typical FOVs with the number of alignment iterations. (a) Convergent tendency in FOV 1, (b) convergent tendency in FOV 0, (c) convergent tendency in FOV 2, (d) convergent tendency in FOV 3, (e) convergent tendency in FOV 5, (f) convergent tendency in FOV 4.

Table 5. Relationship between the Measurement Error of Different Zernike Coefficients and the Misalignment Condition and Corresponding Damping Factor Sequence

Noise of Zernike Coefficient	Damping Factor Sequence (Misalignment Condition)			
(λ = 632.8 nm)	P0 (2λ)	P1 (1λ)	P2 (0.5λ)	P3 (0.1λ)
0.05λ	0.35	0.30	0.22	0.13
0.02λ	0.19	0.16	0.11	0.08

There are two main sources of measurement noise of the Zernike coefficient. The first is the laboratory temperature gradient distribution and random errors caused by airflow. The other is the error caused by the dense fringes collected in the initial CAA stage, and the Zernike coefficient calculation error is introduced here. The fluctuation value of the wavefront aberration and its Zernike coefficient in a single FOV over a period of time are used to evaluate the measurement error of the Zernike coefficient. The standard deviation value of the multiple Zernike coefficient measurement results is taken as the measurement error. After the Zernike coefficient measurement error is injected into the simulation algorithm, a set of damping factor sequences can be obtained, as shown in Table 5. In any iteration of the alignment, the damping factor sequence is sequentially introduced, and the misalignment of each dimension of M2 and M3 can be calculated.

After the rough positioning, the initial wavefront aberrations of the system are measured in six typical FOVs (with FOV 0), as shown in Fig. 13(a). After three alignment iterations, we have the measurement results of the wavefront aberrations of the six FOVs shown in Figs. 13(b) and 13(c).

Figure 14 shows the convergence of the RMS and the 4/5th and 6/7th Zernike coefficients of six typical FOVs during the three adjustment iterations (C4, C5, C6, and C7 represent the Fringe Zernike coefficients Astig x, Astig y, Coma x, and Coma y, respectively).

The experimental results in Figs. 13 and 14 show that after three adjustment iterations, the system wavefront aberrations of an approximately $1.1° \times 1.1°$ square FOV is corrected to the optical design residual level (including surface shape error). With the use of the piecewise DLSM, the success rate of the misalignment improves. The algorithm can be used to obtain the convergence results of the misalignment under the conditions of high initial positioning error and Zernike coefficient measurement uncertainty. Moreover, the number of iterations decreases, and the efficiency of the alignment increases.

Remarkably, the repeating error of the Zernike coefficient as measured with the interferometer is about $0.05\lambda - 0.02\lambda$ ($\lambda = 632.8$ nm) during the experiment. It is observed that the measurement noise of the Zernike coefficient is not constant during the experiment. When the misalignment is large under initial conditions, the interference fringe density and the measurement uncertainty of the Zernike coefficient are large. With the correction of the wavefront aberration of each FOV, the measurement noise of the Zernike coefficient is also reduced. Therefore, the damping factor sequence obtained using the search algorithm should be combined with the measurement error of the Zernike coefficient under different operating conditions and optimized in sections. In this way, the efficiency of the alignment procedure can be further improved.

7. CONCLUSIONS

In this paper, an improved CAA for a nonsymmetric off-axis reflective optical system with freeform surfaces was investigated. Such optical systems generally have a large initial positioning error, resulting in high measurement noise of the Zernike coefficient in the initial alignment step. This phenomenon makes convergence difficult with a conventional LSM. A single-damping-factor algorithm results in low CAA efficiency and the small adjustment being suppressed by the cross talk of the adjustment stage. A method for improving the algorithm for solving the misalignment was proposed. The conclusions of our work have been shown.

Through coupling analysis of the misalignment sensitivity, the search intervals of the damping factor group were obtained. Combined with Monte Carlo simulation analysis, a piecewise damping factors search algorithm was established.

Based on different misalignment thresholds, an adaptive DLSM was introduced. The research showed that the improved algorithm both reduces the sensitivity of the equations to the measurement noise of the Zernike coefficient and expands the range of the initial positioning error threshold.

The simulation and the alignment experiments verified the feasibility and the effectiveness of the above algorithm. The proposed method can be applied to the CAA procedure of nonsymmetric off-axis reflective optical systems. Considering the issues discovered during the experiment, a way to further optimize the search algorithm was provided.

Funding. National Natural Science Foundation of China (61875190, 12003033).

Disclosures. The authors declare no conflicts of interest.

REFERENCES

1. M. L. Lampton, M. J. Sholl, and M. E. Levi, "Off-axis telescopes for dark energy investigations," Proc. SPIE **7731**, 77311G (2010).
2. M. D. Lallo, "Experience with the Hubble Space Telescope: twenty years of an archetype," Opt. Eng. **51**, 011011 (2012).
3. D. Piérot, "Development and performances 3.5 m SiC telescope for the Herschel mission," in *Volume of International Symposium on Optronics in Defense and Security (OPTRO)*, Paris, France, 4 February 2010.
4. H. P. Stahl, M. Postman, W. R. Arnold, Sr., R. C. Hopkins, L. Hornsby, G. E. Mosier, and B. A. Pasquale, "ATLAST-8 mission concept study for 8-meter monolithic UV/optical space telescope," Proc. SPIE **7731**, 77312N (2010).
5. K. Fuerschbach, J. P. Rolland, and K. P. Thompson, "Theory of aberration fields for general optical systems with freeform surfaces," Opt. Express **22**, 26585–26606 (2014).
6. K. Fuerschbach, J. P. Rolland, and K. P. Thompson, "Extending nodal aberration theory to include mount-induced aberrations with application to freeform surfaces," Opt. Express **20**, 20139–20155 (2012).
7. X. Zhao, W. Jiao, Z. Liao, Y. Wang, and J. Chen, "Study on computer-aided alignment method of a three-mirror off-axis aspherical optical system," Proc. SPIE **7656**, 76566M (2010).
8. S. Kim, H.-S. Yang, Y.-W. Lee, and S.-W. Kim, "Merit function regression method for efficient alignment control of two-mirror optical systems," Opt. Express **15**, 5059–5068 (2007).
9. J. P. McGuire, Jr. and R. P. Korechoff, "Optical alignment and test of Wide-Field/Planetary Camera-II," Proc. SPIE **1996**, 159–174 (1993).
10. G. F. Hartig, J. H. Crocker, and H. C. Ford, "On-orbit alignment of the spectrograph channels of the corrective optics space telescope axial replacement (COSTAR)," Proc. SPIE **298**, 1181–1191 (1994).
11. R. Jedrzejewski, G. F. Hartig, and P. Jakobsen, "On-orbit alignment of the FOC channel of COSTAR," Proc. SPIE **2198**, 1192–1201 (1994).
12. M. L. Kaplan, K. I. MacFeely, R. B. Slusher, and R. F. Cahill, "COSTAR Phase II alignment description," Proc. SPIE **1996**, 227–236 (1993).
13. R. Geyl, "Design and fabrication of a three mirror flat field anastigmat for high resolution earth observation," Proc. SPIE **2210**, 739–749 (1994).
14. M.-T. Velluet, M. Sechaud, V. Michau, and P.-Y. Madec, "Automatical alignment system for telescopes," Proc. SPIE **2210**, 747–751 (1994).
15. J. W. Figoski, "The Quick Bird telescope: the reality of large, high-quality, commercial space optics," Proc. SPIE **3379**, 22–30 (1999).
16. B. Zhang, X. Zhang, C. Wang, and C. Han, "Computer-aided alignment of the complex optical system," Proc. SPIE **4231**, 67–72 (2000).
17. X. Yang, X. Zhang, and C. Han, "Alignment of a three-mirror off-axis aspherical optical system by using gradual aberration optimization," Acta Opt. Sinica **24**, 115–120 (2004).
18. K. P. Thompson, "Description of the third-order optical aberrations of near-circular pupil optical systems without symmetry," J. Opt. Soc. Am. A **22**, 1389–1401 (2005).
19. K. P. Thompson, "Multinodal fifth-order optical aberrations of optical systems without rotational symmetry: spherical aberration," J. Opt. Soc. Am. A **26**, 1090–1100 (2009).
20. K. Fuerschbach, J. P. Rolland, and K. P. Thompson, "Nodal aberration theory applied to freeform surfaces," in *Classical Optics* (Optical Society of America, 2014), paper ITh2A.5.
21. B. Eegholm, S. Wake, Z. Denny, P. Dogoda, D. Poulios, B. Coyle, P. Mule, J. Hagopian, P. Thompson, L. Ramos-Izquierdo, and B. Blair, "Global ecosystem dynamics investigation (GEDI) instrument alignment and test (Invited Paper)," Proc. SPIE **11103**, 1110308 (2019).
22. P. Coulter, R. G. Ohl, P. N. Blake, B. J. Bos, W. L. Eichhorn, J. S. Gum, T. J. Hadjimichael, J. G. Hagopian, J. E. Hayden, S. E. Hetherington, D. A. Kubalak, K. F. Mclean, J. McMann, K. W. Redman, H. P. Sampler, G. W. Wenzel, and J. L. Young, "A toolbox of metrology-based techniques for optical system alignment (Invited Paper)," Proc. SPIE **9951**, 995108 (2016).
23. K. Fuerschbach, G. E. Davis, K. P. Thompson, and J. P. Rolland, "Assembly of a freeform off-axis optical system employing three φ-polynomial Zernike mirrors," Opt. Lett. **39**, 2896–2899 (2014).
24. C. Wang, X. Zhang, L. Wang, J. Zhang, and J. Zhang, "Adjustment of three-mirror off-axis freeform system," Acta Opt. Sinica **33**, 1208001 (2013).
25. D. Gong, H. Wang, and T. Tian, "Computer-aided alignment of off-axis three-mirror imaging spectrometer system," Proc. SPIE **8910**, 89100Z (2013).
26. M. P. Rimmer, "A computer aided optical alignment method," Proc. SPIE **1271**, 363–368 (1990).